ACS NANO

www.acsnano.org

ARTICLE

Single-Molecule Imaging Using Atomistic Near-Field Tip-Enhanced Raman Spectroscopy

Pengchong Liu, Dhabih V. Chulhai,[†] and Lasse Jensen*

Department of Chemistry, Pennsylvania State University, University Park, Pennsylvania 16802, United States

Supporting Information

ABSTRACT: **Advances in tip-enhanced Raman spectroscopy (TERS) have demonstrated ultrahigh spatial resolution so that the vibrational modes of individual molecules can be visualized. The spatial resolution of TERS is determined by the confinement of the plasmon-induced field in the junction; however, the conditions necessary for achieving the high spatial confinement required for imaging individual molecules are not fully understood. Here, we present a systematic theoretical study of TERS imaging of single molecules, using a hybrid atomistic electrodynamics−quantum mechanical method. This approach provides a consistent treatment of the molecule and the plasmonic near field under conditions where they cannot be treated separately. In our simulations, we demonstrate that TERS is capable of resolving intricate molecule vibrations with atomic resolution, although we find that TERS images are extremely sensitive to the near field in the junction. Achieving the atomic resolution requires the near field to be confined within a few ångstroms in diameter and the near-field focal plane to be in the molecule plane. Furthermore, we demonstrate that the traditional surface selection rule of Raman spectroscopy is altered due to the significant field confinement that leads to significant field-gradient effects in the Raman scattering. This work provides insights into single-molecule imaging based on TERS and Raman scattering of molecules in nanojunctions with atomic dimensions.**

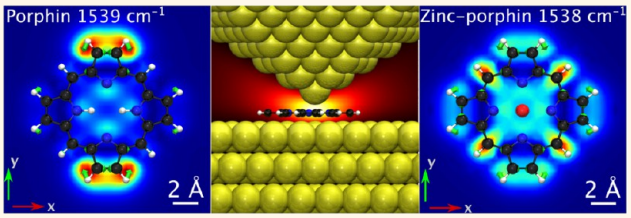

KEYWORDS: *tip-enhanced Raman spectroscopy, single-molecule imaging, near-field confinement, gap plasmons, field-gradient effect, resonant Raman scattering*

Tip-enhanced Raman spectroscopy (TERS) integrates the surface-enhanced Raman spectroscopy (SERS) with scanning probe microscopy (SPM).[1−3] The nanostructure of a noble metal SPM tip is optically excited to generate localized surface plasmon resonances (LSPRs). The LSPR induces a strong electromagnetic field that is confined within the tip−substrate junction, which drastically enhances ($\sim 10^8$) the Raman scattering signals of the specimen located in the junction. Due to the extremely high sensitivity and spatial resolution, TERS is very promising for applications in numerous fields, including materials engineering,[4−8] electrochemistry and catalysis,[9−15] and biotechnology.[16−20]

Precise control of the field within the SPM junction at cryogenic temperatures has led to higher and higher spatial resolution of TERS.[21−29] Recently, TERS imaging of a single *meso*-tetrakis(3,5-di-*tert*-butylphenyl)porphyrin molecule (H_2TBPP) with a subnanometer resolution was reported, where the structural profile of the molecule was visualized by mapping the TERS signals while scanning across the molecule.[30] Later, it was demonstrated that TERS is able to distinguish between different molecules with similar structures, adsorbed adjacent to each other.[31] Moreover, using a simultaneous TERS and STM imaging technique, it is possible to resolve subtle differences of adsorbates, such as conformational differences.[32] In these studies, lateral resolutions of only a few ångstroms have been achieved.

Along with the great strides in experiments comes an urgent need for in-depth investigations of the physical mechanism underlying the spatial resolution of TERS.[31,32] Computer simulation is a necessary approach to rationalizing experimental findings and to a complete understanding of TERS imaging. Since the spatial resolution of TERS imaging is determined by the confinement of the field that is induced by the sharp tip,[22,33,34] it is crucial for TERS theories to accurately describe this confined field in the junction.

One of the earliest efforts to model the TERS used an arbitrary Gaussian-confined near field and described its interaction with molecules using time-dependent density functional theory (TDDFT).[30,35] This model was later employed to visualize the vibrational modes of water with submolecular features.[36] Although this model was successful in reproducing the TERS images obtained in experiments, it provides no mechanism for generating the highly confined fields necessary for the TERS resolution. Futhermore, in a typical TERS setup, the size of the junction is within the quantum effects regime where the

Received: March 24, 2017
Accepted: May 2, 2017
Published: May 2, 2017

DOI: 10.1021/acsnano.7b02058
ACS Nano 2017, 11, 5094−5102

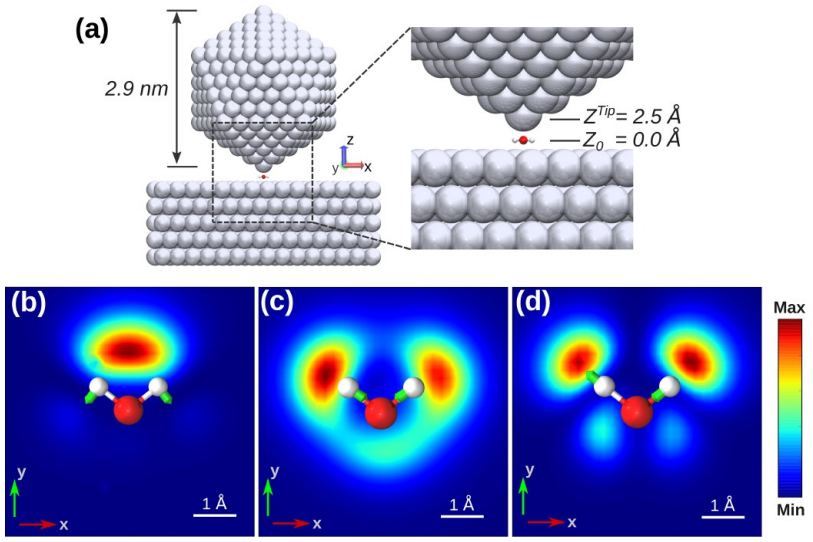

Figure 1. (a) Ag_{561} icosahedron with a diameter of 2.9 nm is used as the SPM tip, and a water molecule sits flat on the silver XY plane. Simulated TERS images of the water molecule at different vibrational modes: (b) bending mode at 1600 cm^{-1}; (c) symmetric stretching mode at 3676 cm^{-1}; (d) antisymmetric stretching mode at 3776 cm^{-1}. The dimensions of each TERS image are 6 Å × 6 Å. The plot dimension and the color scale bar are shared by all TERS images of water in this work unless otherwise stated.

plasmonic responses are significantly modified.[37−41] Microscopic details of the metallic junction are needed for an accurate description of the plasmon-induced near field in the quantum size regime and thereby a complete and accurate description of TERS.[41−43] Both quantum mechanical models[43] and classical models[44] have demonstrated that atomic features in the junctions can lead to such high field confinement. Quantum mechanical simulations have shown that such high resolution is possible based on a chemical enhancement mechanism but did not consider the localized near field, which typically dominates the enhancement.[45] Atomistic electrodynamics represents each atom of a metallic nanoparticle by an atomic polarizability and, thus, enables a precise control of the local environment of the nanoparticle.[46,47] As a result, the plasmonic properties due to quantum mechanical effects in a subnanometer gap are accurately captured by the atomistic electrodynamics model.[42,48] Therefore, atomistic electrodynamics combined with a TDDFT description of the molecules provides a consistent treatment of the molecules and the nanojunction and, thus, is well-suited for describing high-resolution TERS.

Herein, we present a systematic study of single-molecule TERS imaging with atomic resolution using a hybrid atomistic electrodynamics−quantum mechanical approach.[42] We observe in simulations that the atomic resolution of TERS imaging arises from the extreme confinement of the near field, which is determined by the incident light energy. The field maximum height relative to the molecule plane, which we define as the near-field focal plane, is found to have significant effects on the TERS images, especially for nonplanar molecules. We show that a field confinement of a few ångstroms and a near-field focal plane in the molecule plane are necessary for generating high-resolution images in TERS. The highly confined field also results in strong local field gradient, which changes the selection rule of Raman spectroscopy.[49,50] We are able to visualize these field-gradient-enhanced vibrations in the simulated TERS images. For resonant Raman scattering, we are able to resolve different vibrational modes of one porphyrin molecule with atomic features and to distinguish similar vibrations associated with two different porphyrins based on the transition dipole moment between electronic states.

RESULTS AND DISCUSSION

In our simulation model (Figure 1 a), a water molecule is placed flat on a silver plane (XY) with a vertical separation of 2.5 Å. Previous simulations[36] demonstrated high-resolution TERS images for water, and thus this system provides a good benchmark system. We consider the molecule plane to pass through the origin of the Z axis (Z_0 = 0.0 Å). The SPM tip is represented by the vertex of a silver icosahedral nanoparticle (Ag_{561}). In the specific case of Figure 1, the tip of the nanoparticle is Z^{Tip} = 2.5 Å above the molecule plane and is excited by an incident light of 3.09 eV. The effects of the incident light energy and the tip-to-sample height will be addressed later. The silver nanoparticle is moved by a small step size (0.2 Å) across an area covering the molecule. TERS intensities, represented by the differential cross sections,[51] are calculated at each step. Only the *zz* component of the polarizability tensor is used for the intensity calculations, as it resembles experimental setups of perpendicular plane-polarized light and back scattering, and sample molecules are assumed to exhibit no rotation. Mapping the intensities for each vibrational mode (see Figure S2 for full spectra), we obtain the TERS images of the water molecule, as shown in Figure 1b−d. Our results qualitatively agree with the images presented in ref 36, but have a few nontrivial differences. For the bending mode, the hot-spots are roughly elliptical instead of the dumbbell shape reported in ref 36. Also, the hot-spots are located between the two hydrogen atoms, with no prominent feature around the oxygen atom. For the symmetric and antisymmetric stretching modes, we observe slight symmetry breaking in the TERS images. This is likely due to the difference in the curvatures of the tip along the X and Y axes. Along the Y axis, the edge of the icosahedron is in the +Y direction, while the facet is in the −Y direction. Along the X axis both directions see an edge, but the projection line of these two edges onto the imaging plane is not parallel with the X axis. The variance in the tip curvature gives rise

DOI: 10.1021/acsnano.7b02058
ACS Nano 2017, 11, 5094−5102

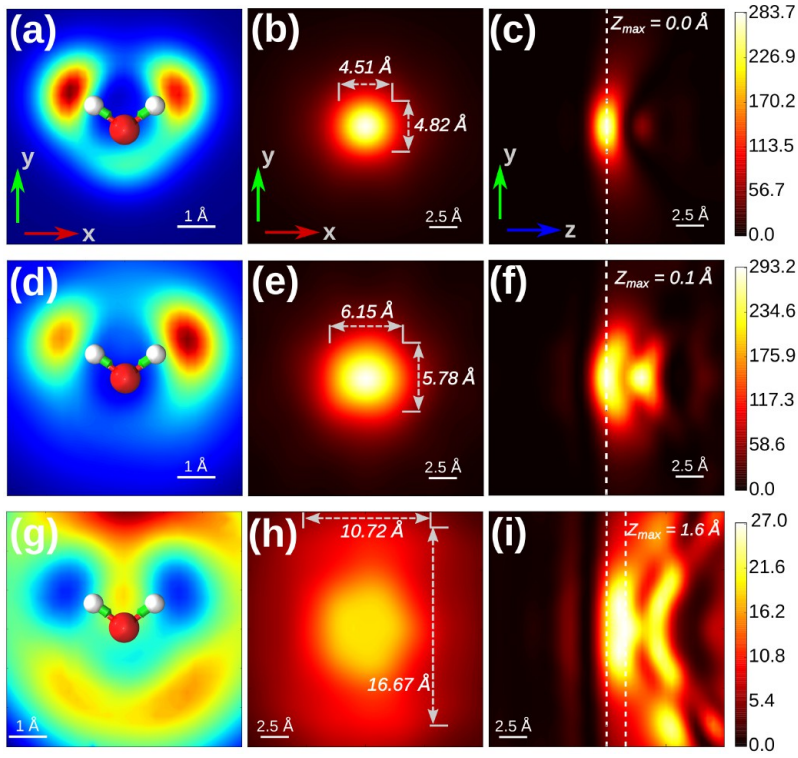

Figure 2. TERS images of the symmetric stretching mode and field enhancement ($|E|^2/|E_0|^2$) distributions with different incident light energies: (a–c) 3.09 eV, (d–f) 3.41 eV, (g–i) 3.59 eV. For the field enhancement map in the molecule plane (b, e, h), the fwhm's along the X and Y axes are noted in ångstroms. For the field enhancement map in the YZ plane (c, f, i), the water molecule plane, Z_0 = 0 Å, is represented by the white dashed line on the left side; the maximum positions of the field on the Z axis are represented by the dashed line on the right side, noted as Z_{max}. The dimensions of each field distribution plot are 20 Å × 20 Å.

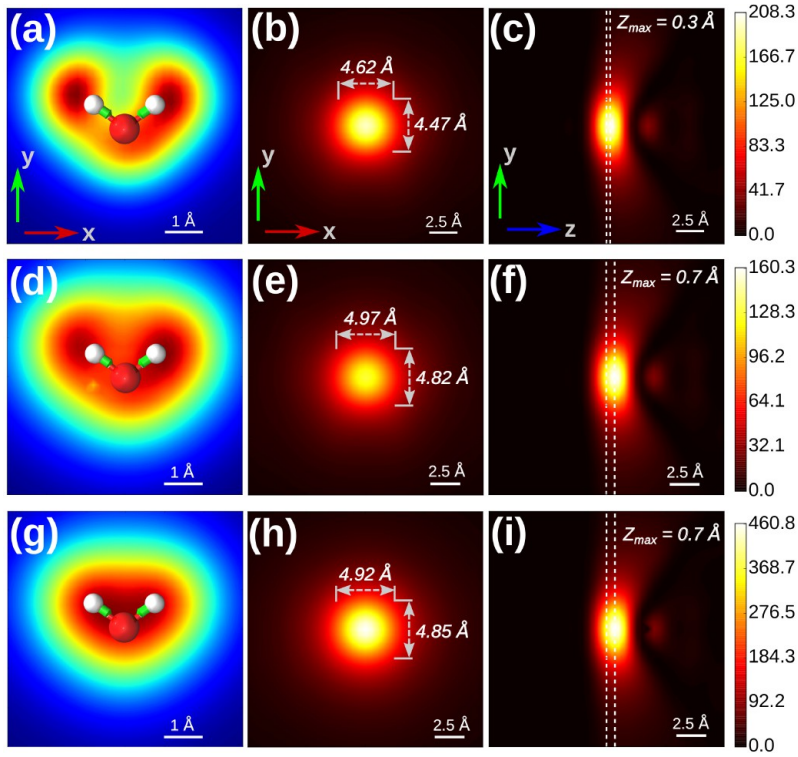

Figure 3. TERS images of the symmetric stretching mode and field distributions with a tip-to-sample height of Z^{Tip} = 3.0 Å (a–c) and Z^{Tip} = 3.5 Å (d–f). The same setup as in Figure 1a is used for the first two rows. The bottom row (g–i) corresponds to the large nanoparticle (Ag_{2057}), with Z^{Tip}_{large} = 3.5 Å.

DOI: 10.1021/acsnano.7b02058
ACS Nano 2017, 11, 5094–5102

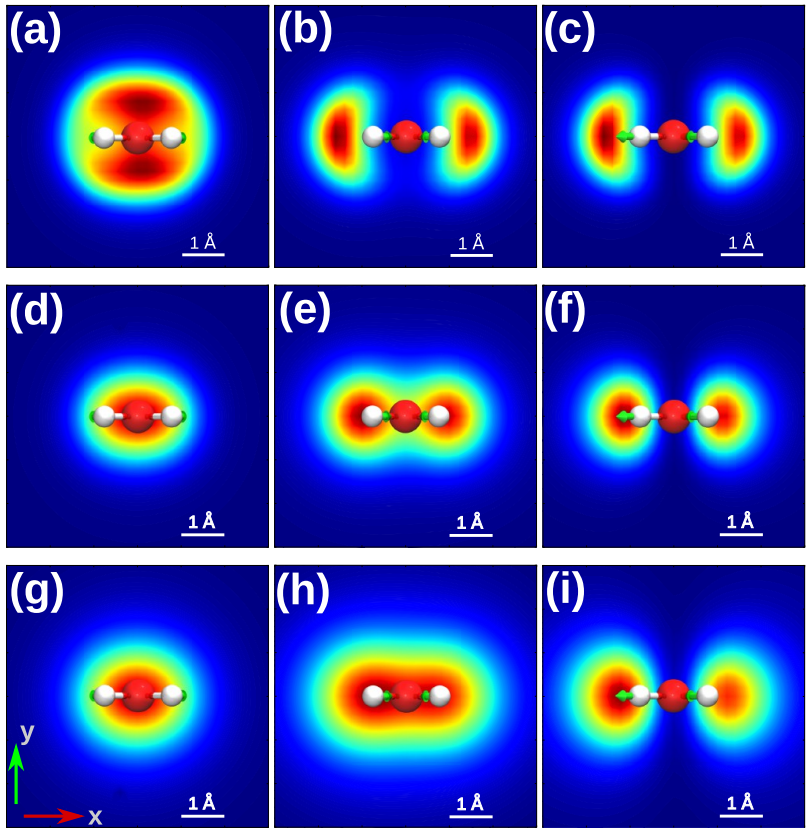

Figure 4. TERS images of the vertical water molecule. The oxygen atom is at the bottom, placed at Z^O = 0.0 Å, and the height of hydrogen atoms are both Z^H = 0.60 Å. Tip-to-oxygen distance is 2.5 Å (a–c, field maximum at Z_{max} = 0.0 Å), 3.0 Å (d–f, Z_{max} = 0.3 Å), and 3.5 Å (g–i, Z_{max} = 0.7 Å). The first column (a, d, g) corresponds to the bending mode; the second column (b, e, h) corresponds to the symmetric stretching mode; the third column (c, f, i) corresponds to the antisymmetric stretching mode.

to asymmetry in the near-field distribution on the imaging plane and, consequently, asymmetric interactions with the molecule.

For the aforementioned junction structure, we examine the effect of field confinement on TERS spatial resolution by varying the energy of the incident light. Three energies are selected for case studies: 3.09, 3.41, and 3.59 eV, which spans from the onset of the nanoparticle absorption band to the peak (Figure S1). The near-field intensity ($|E|^2/|E_0|^2$) is calculated from induced atomic dipoles of the metal system on a numerical grid (step size 0.2 Å) with a probe radius of 1.50 Å.[48] To quantify the field confinement, the full widths at half maxima (fwhm's) of the field enhancement along the X and Y axes are obtained directly from the field grid without any curve fitting (see Figure S3 for the line shapes of the field). For conciseness, only the symmetric stretching mode is shown in the following discussions on water, as the other modes exhibit the same trend (Figures S4 and S5). As is shown in Figure 2, the TERS image of the best resolution is generated by the incident light of about 3.09 eV. The distribution of near-field intensity has fwhm's slightly less than 5 Å, and the field maximum is located exactly on the molecule plane (Z_{max} = 0.0 Å). With the 3.41 eV incident light, the near field is less confined, of which the fwhm's are about 6 Å. The TERS image is blurred, relatively speaking, compared to the 3.09 eV case, despite the fact that the field intensity is slightly higher. In the 3.59 eV case (plasmonic peak), the field is significantly less confined and the intensity decreases by an order of magnitude, which leads to the loss of atomic features in the corresponding TERS image.

An atomically sharp tip, as modeled in this work, is found experimentally to be able to trap optical fields in a subnanometer cavity at cryogenic temperatures.[52] Such extreme confinement of the field is well reproduced in our model, represented by fwhm's in Figure 2. For an isolated plasmonic nanoparticle, the enhanced field localized on the sharp points of the structure is caused by the plasmonic resonance.[53] However, for a plasmonic dimer with a small gap (in this case, substrate and tip nanoparticle), the strongest field enhancement within the junction occurs at a lower energy than the single-nanoparticle plasmonic resonance,[40] which arises from a metallic screening in the junction ("lightning rod effect").[43,54] When the dimer system is excited at the single-nanoparticle plasmon energy, the intensity of the induced near field within the tip–substrate junction decreases and the "effective localization area" enlarges (*i.e.*, less confined).[43] Consequently, the obtained TERS images under the single-nanoparticle plasmonic resonance do not retain the desired resolution (Figure 2g). In short, the resolution of TERS is extremely sensitive to the confinement of the field. With a carefully controlled incident light energy, an atomically sharp tip is able to confine the field in an area of about 5 Å in diameter (fwhm), which suffices to unravel atomic features for TERS images. The confinement of the field cannot reach any significantly smaller area according to the atomistic electrodynamics model.

Also shown in Figure 2, the height of the near-field maximum (Z_{max}) in addition to the confinement area changes with the incident light energy. For the TERS images of the best resolution, the near-field maximum is exactly in the molecule plane (Z_{max} = 0

DOI: 10.1021/acsnano.7b02058
ACS Nano 2017, 11, 5094–5102

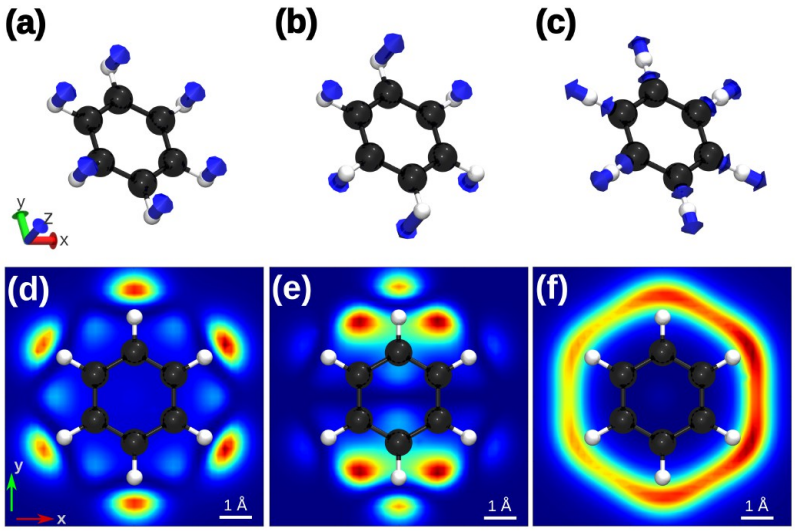

Figure 5. Selected normal modes and their respective TERS images of the benzene molecule: (a and d) 664 cm^{-1}, (b and e) 835 cm^{-1}, (c and f) 988 cm^{-1}. The carbon vibrations are not intense enough to be seen in (a) and (b). The schematics of molecular vibrations (a–c) are rotated slightly for a clearer view of out-of-plane motions. The dimensions of each TERS image are 8 Å × 8 Å.

Å). To better understand this effect, we slightly retract the tip without breaking the junction (Figure 3a–f) and keep the incident energy of 3.09 eV for the same field confinement. We find that the height of the near-field maximum changes with the height of the nanoparticle tip (Figure 3c and f) and that the height of the field maximum determines the resolution of the TERS images. With Z_{max} = 0.3 Å, the desired pattern of the TERS image can still be roughly preserved (Figure 3a). But at Z_{max} = 0.7 Å the resolution drops significantly (Figure 3d).

In order to rule out the effect of the reduced field intensity in the molecule plane while retracting the tip, the size of the nanoparticle is increased to generate a stronger field. Using the large nanoparticle (Ag_{2057}, 4.6 nm in diameter) that is also excited at 3.09 eV, we are able to increase the near-field intensity while keeping the tip curvature, field-confinement area, and field maximum height unaltered (Figure 2h and i). In this regard, we find that the increased field intensity does not lead to better imaging resolution. Even for the stronger field, it still requires the field maximum to be in the molecule plane to achieve the atomic resolution (Figure S7). In the simulations presented above, the field maximum position is consistently in or higher than the molecule plane, which adheres to the presumption of no chemical bonding between the tip and the molecule. We also push the nanoparticle closer to the molecule to have the near-field maximum underneath the molecule plane (Z_{max} = −0.2 Å). The obtained TERS images retain the desired resolution (Figure S6). The field maximum height, Z_{max}, can be considered as the plane of focus for the near field in TERS imaging apparatus. The sharpest resolution of TERS images is obtained in the focal plane, which is preferred to overlap with the molecule plane.

However, the molecule adsorbed on the metal substrate is very likely, in reality, to have a more complex structure than a simple plane. The focal plane height is then expected to affect the TERS images in other aspects than the resolution alone. We explore these aspects by simulating a water molecule placed perpendicular to the substrate, where the oxygen atom is in the original plane (Z^O = 0.0 Å) and the hydrogen atoms are closer to the tip (Z^H = 0.60 Å). Each of the aforementioned focal planes (Z_{max} = 0.0, 0.3, 0.7 Å) are located on the oxygen atom, in between the oxygen and the hydrogen, or roughly on the hydrogen atoms. As is shown in Figure 4, the three focal planes all lead to atomistically resolved TERS images. However, each normal mode of water behaves differently with respect to changes of focal plane height, and the identity of water by its TERS images is not as clear as it was in the parallel case. For the bending mode (Figure 4a, d, and g), the hot-spots evolve from two overlapping ovals into a single oval as the focal plane is moved higher. The symmetric stretching mode has two separate lobes located in the vicinity of the H atoms when the focal plane is on the oxygen atom (Figure 4b). While elevating the focal plane, the two lobes expand toward the center and eventually merge into one ellipse on top of the projection of the molecule (Figure 4e and h). The antisymmetric stretching mode has almost the same TERS image as the symmetric mode (Figure 4c) at first; however, rather than merging into one ellipse, the two lobes consistently expand outward as the focal plane moves higher. The above analyses indicate that small changes in the focal plane height may exert dramatic effects on the TERS image patterns. To ensure the best resolution, the focal plane is kept on the molecule plane (Z_{max} = 0.0 Å) in the following discussions.

The highly confined field in the TERS junction brings about strong field gradients (FGs), which may change the selection rules for plasmon-enhanced Raman spectroscopies.[55−59] To explore the FG effects in TERS, we simulate the TERS images of benzene. Three FG active normal modes of benzene are selected in this study, which are associated with the symmetry type a_{2u} (ν_{11}, 664 cm^{-1}), e_{1g} (ν_{10}, 835 cm^{-1}), and a_{1g} (ν_1, 988 cm^{-1}). In the first two modes, the molecule vibrations are out-of-plane. As reported in detail in ref 59, the induced dipoles of the 664 cm^{-1} mode arise from FG contributions through the electric dipole−quadrupole term ($|E'|^2 \cdot |\nabla E|^2 + |\nabla E'|^2 \cdot |E|^2$, correlated field and FG enhancement mechanism); the 835 cm^{-1} mode is enhanced by FG through the quadrupole−quadrupole term ($|\nabla E'|^2 \cdot |\nabla E|^2$, pure FG term); the 988 cm^{-1} mode exhibits contributions from both the dipole−dipole term and the quadrupole−quadrupole term ($|E'|^2 \cdot |E|^2 + |\nabla E'|^2 \cdot |\nabla E|^2$, separate field and FG contributions). These three modes are explicitly depicted in Figure 5a–c.

In the 664 cm^{-1} mode (Figure 5a and d), the six hydrogen atoms are symmetrically vibrating vertical to the carbon ring. The corresponding TERS image preserves the symmetry, where the

DOI: 10.1021/acsnano.7b02058
ACS Nano 2017, 11, 5094−5102

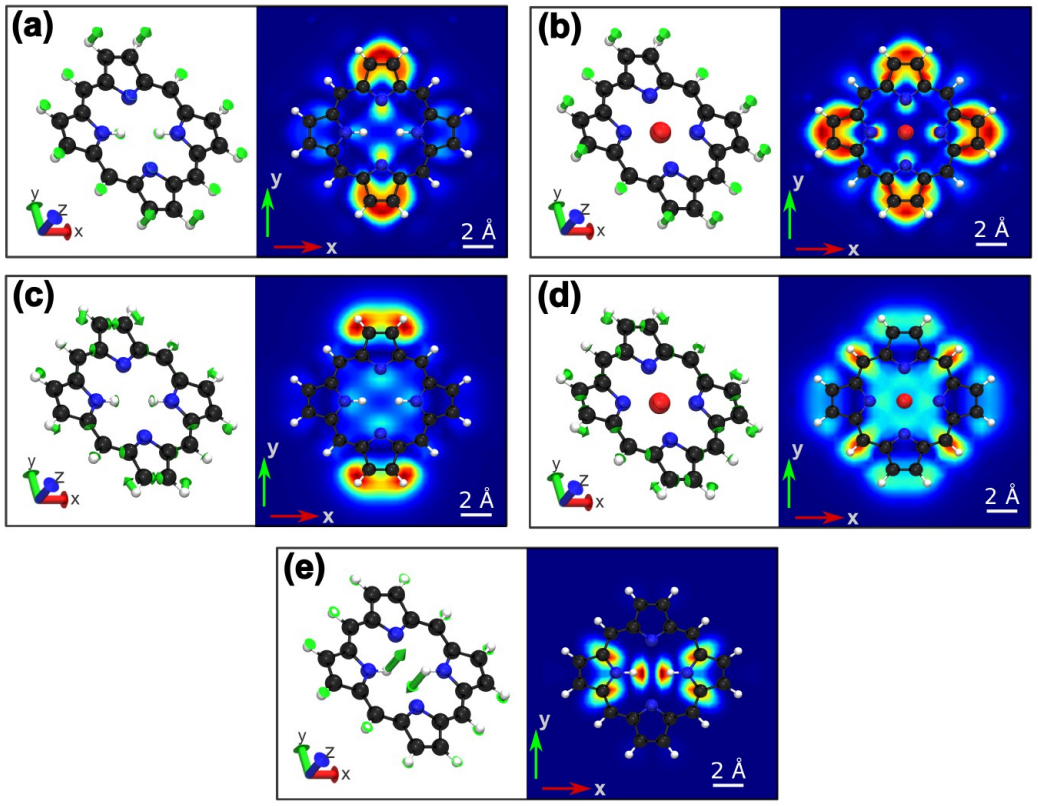

Figure 6. Selected normal modes and their respective TERS images of porphyrin molecules: (a) 683 cm^{-1} for porphin, (b) 692 cm^{-1} for ZnP, (c) 1539 cm^{-1} for porphin, (d) 1538 cm^{-1} for ZnP, and (e) 678 cm^{-1} for porphin. (a) and (b), and (c) and (d) are pairs of similar vibrational modes in porphin and ZnP. The scanned area of each TERS image is 16 Å × 16 Å. The schematics of molecular vibrations (left side of each subfigure) are rotated slightly for a clearer view of out-of-plane motions.

hot-spots are six lobes located outside the molecule in close vicinity to the H atoms. The less prominent hot-spots in between two neighboring H atoms are ascribed to the relatively weak carbon motions that are coupled with the hydrogen motions but in the opposite direction. In the 835 cm^{-1} mode (Figure 5b and e), the H atoms are vibrating in two opposite directions, with the 1- and 4-H motions being the strongest. Meanwhile, each C atom is vibrating in the same direction as its attached H atom. As a result, the TERS image shows an overall dipolar pattern. As for the 988 cm^{-1} mode, the simulated TERS image captures the "ring breathing" feature of the vibration, leading to a continuous hexagonal pattern (Figure 5c and f). The hot-spots in the TERS images of benzene (as well as water) appear to be next to the atom projections on the XY plane rather than on top of them. Given that the maximum point of the near field in the imaging plane is at the exact spot of the tip atom (Figure S3), when the tip scans through the area surrounding a certain chemical bond, the bond itself sees a strong field gradient. We also note that the asymmetries of these TERS images are related to the tip curvature difference. The simulations of benzene clearly demonstrate that TERS is capable of detecting and visualizing FG active vibrational modes.

To extend the study from nonresonant to resonant TERS, we carry out simulations of TERS imaging of simple porphyrin molecules. The two model molecules are porphin and zinc porphin (ZnP). TDDFT calculations in a vacuum show that the $Q_y(0, 0)$ transition of the two molecules are both at 2.29 eV. Additionally, the $Q_x(0, 0)$ transition of ZnP is degenerate with its $Q_y(0, 0)$ transition. To match this excitation energy for resonant Raman while maintaining a highly confined field in the junction, we use a Au_{2057} icosahedron as the tip and gold substrate with a Au(111) surface. The incident light energy of 2.29 eV corresponds to halfway on the low-energy edge of the absorption band of the gold nanoparticle (see Figure S1 for the absorption spectrum). The induced near field is confined within about 5.6 Å in diameter (fwhm), while the maximum is at Z_{max} = 0.1 Å (Figure S8). The field-confinement conditions resemble those for the nonresonant TERS images of the best resolution (Figure 2) and thereby suffice to resolve atomic features in the simulated TERS images.

The experimental TERS images of different porphyrin (H_2TBPP) vibrational modes appeared similar to each other, with four lobes of hot-spots located symmetrically at the four phenyl groups.[30] However, our simulated TERS images of the porphin are clearly distinct from each other (Figure 6a,c,e). Moreover, similar vibrational modes shared by porphin and ZnP lead to very different patterns in the TERS images. Specifically, the 683 cm^{-1} mode of porphin and 692 cm^{-1} mode of ZnP correspond to the same symmetric out-of-plane motions of the outer hydrogen atoms (Figure 6a and b). Similarly, the 1539 cm^{-1} mode of porphin and the 1538 cm^{-1} mode of ZnP have the same pattern of in-plane atomic motions (Figure 6c and d). For each pair of vibrational modes, we find that the outline shape of the patterns in the TERS images remains the same, but the distribution of hot-spots differs. The TERS images of porphin exhibit an overall dipolar pattern along the Y direction, while ZnP gives rise to a 4-fold symmetric pattern. As stated above, the transition dipole moment (TDM) of porphin under the specific

DOI: 10.1021/acsnano.7b02058
ACS Nano 2017, 11, 5094−5102

resonance condition is completely along the Y axis [$Q_y(0, 0)$], while the TDM of zinc porphin has almost equal contributions from both the X and Y directions [$Q_x(0, 0) + Q_y(0, 0)$]. Therefore, we ascribe the symmetry in resonant TERS images to the direction of the TDM. If the two central hydrogens of porphin were aligned on the X axis, one would expect the TERS image to be rotated accordingly. In fact, the hydrogen tautomerization of porphyrin molecules has been reported to take place in low-temperature STM experiments with a small bias (<1.5 V), and the activation barrier depends on the specific chemical species and the substrate.[60,61] Therefore, we believe that hydrogen tautomerization is the root of the 4-fold symmetry obtained in the experimental TERS imaging of H_2TBPP in ref 30. As for the vibrational mode associated with strong central hydrogen motions (Figure 6 e), the TERS image has hot-spots inside the porphin ring and around the carbon atoms whose motions are coupled to the hydrogen vibrations. The clear distinction between vibrational modes with atomic details presented in this work has not been observed in previous experiments or theoretical simulations.[30,35] These simulations demonstrate the ability of TERS imaging to atomistically resolve different vibraional modes under resonant Raman conditions.

CONCLUSION

In this work we simulated single-molecule TERS imaging with atomic resolution using a hybrid atomistic electrodynamics−quantum mechanical approach. We showed that an atomically sharp tip in a quantum size junction confines the plasmon-induced near field within a few ångstroms in diameter (fwhm), and this confinement is closely related to the incident light energy. Using water as a simple model system, we observed that the resolution of TERS images is extremely sensitive to the field confinement. The field confinement of ∼5 Å in fwhm's is narrow enough to resolve each vibrational mode of a single molecule with atomistic details. We also demonstrated the importance of the near-field focal plane of TERS, which is defined as the field maximum height. The focal plane is required, in principle, to overlap with the molecule plane to obtain the best resolution. For nonplanar molecular geometries, the effect of focal plane height becomes intricate. A small change in the focal plane may lead to a significantly different TERS image, and this dependence varies from mode to mode. Moreover, by visualizing the field-gradient active modes of benzene, we conclude that field-gradient effects are implicated in the TERS images. Finally, it is illustrated in the porphyrin simulations that TERS imaging is also able to atomistically resolve different vibrational modes under resonant Raman conditions, where hot-spot distributions in the images are determined by the electronic transition dipole moments. In addition to the theoretical insights, this work highlights the necessity of accurately describing the near field in the quantum size junction for TERS simulations. The atomistic electrodynamics approach adopted in this work provides a mechanism to generate the plasmon-induced field and to describe plasmon−molecule interactions, which can be applied for more general TERS studies in the future.

METHODS

A locally modified version of the Amsterdam Density Functional (ADF) program package[62−64] was used to carry out the calculations. The Becke−Perdew (BP86)[65,66] exchange−correlation functional and the triple-ζ polarized (TZP) Slater-type basis set from the ADF library were used. The geometries of the sample molecules were optimized with a small frozen core in the absence of the plasmonic nanostructure. The vibrational frequencies and normal modes were calculated analytically without scaling. Differential cross sections ($d\sigma/d\Omega$) of Raman scattering represent the TERS intensities in this work. To resemble the experimental setup, only the zz component of the polarizability tensor was used to calculate the differential cross section, which is given by[51,67]

$$\frac{d\sigma}{d\Omega} = \frac{\pi^2}{\epsilon_0^2}(\tilde{\nu}_{in} - \tilde{\nu}_p)^4 \frac{h}{8\pi^2 c\tilde{\nu}_p} \frac{|\alpha'_{zz,p}|^2}{1 - \exp(-hc\tilde{\nu}_p/k_B T)} \quad (1)$$

where $\tilde{\nu}_{in}$ is the frequency of incident light and $\tilde{\nu}_p$ is the frequency of the pth vibrational mode. $\alpha'_{zz,p}$ is the zz component of molecular polarizability derivative with respect to the pth vibrational mode. The molecular polarizabilities were calculated using the AOResponse module implemented in ADF with a excited-state lifetime of Γ = 0.1 eV.[67−71] The polarizability derivatives are obtained by numerical three-point differentiation. This is done by calculating the polarizabilites for molecular geometries in a plus and a minus direction of a certain normal mode. High numerical qualities for TDDFT calculations are recommended to obtain smooth TERS images. TERS cross sections are obtained assuming T = 298 K.

All metal atoms were treated with the discrete interaction model (DIM).[46,47] The icosahedron nanoparticles were constructed using FCC unit cells. The substrates were constructed as a large block of silver (or gold) unit cells, and molecules were placed on the (111) surface. The frequency-dependent complex dielectric functions of silver and gold were obtained from Johnson and Christy.[72] The nanoparticle was moved across an area large enough to cover the sample molecule (6 Å × 6 Å for water, 8 Å × 8 Å for benzene, and 16 Å × 16 Å for porphyrins). The step size for scanning was 0.2 Å. Smaller step sizes such as 0.1 Å were found to have no significant effect on the TERS images other than smoothness. For the purpose of reducing computational cost of the porphyrin simulations, only one quadrant of each simulated image was calculated and then expanded to full size in accordance with the rotational symmetry of the molecule. The asymmetry in the TERS images due to the tip curvature variation as is for water and benzene was consequently removed.

All molecular geometries and vibrations were rendered using the Visual Molecular Dynamics (VDM) 1.9.3 software.[73] Molecular vibrations were visualized by atomic displacement vectors obtained from normal mode coordinates.

ASSOCIATED CONTENT

Supporting Information

The Supporting Information is available free of charge on the ACS Publications website at DOI: 10.1021/acsnano.7b02058.

Absorption spectra of single nanoparticles; TERS and regular Raman spectra of single molecules; line shapes of the near field within the nanojunction; TERS images of water bending and antisymmetric stretching modes under different field-confinement conditions; TERS images of water with the focal plane underneath the molecule plane; near field generated by the gold nanojunction (PDF)

AUTHOR INFORMATION

Corresponding Author

*E-mail: jensen@chem.psu.edu. Phone: +1-814-867-1787.

ORCID

Lasse Jensen: 0000-0003-1237-5021

Present Address

†Department of Chemistry, University of Minnesota, 207 Pleasant Street SE, Minneapolis, Minnesota 55455, United States.

Notes

The authors declare no competing financial interest.

DOI: 10.1021/acsnano.7b02058
ACS Nano 2017, 11, 5094−5102

ACKNOWLEDGMENTS

P.L., D.V.C., and L.J. acknowledge the support from the National Science Foundation Center for Chemical Innovation dedicated to Chemistry at the Space-Time Limit (CaSTL) Grant CHE-1414466. Portions of this work were conducted with Advanced CyberInfrastructure computational resources provided by The Institute for CyberScience at The Pennsylvania State University (http://ics.psu.edu).

REFERENCES

(1) Huang, T.-X.; Huang, S.-C.; Li, M.-H.; Zeng, Z.-C.; Wang, X.; Ren, B. Tip-Enhanced Raman Spectroscopy: Tip-Related Issues. *Anal. Bioanal. Chem.* **2015**, *407*, 8177−8195.

(2) Jiang, N.; Kurouski, D.; Pozzi, E. A.; Chiang, N.; Hersam, M. C.; Duyne, R. P. V. Tip-Enhanced Raman Spectroscopy: From Concepts to Practical Applications. *Chem. Phys. Lett.* **2016**, *659*, 16−24.

(3) Zrimsek, A. B.; Chiang, N.; Mattei, M.; Zaleski, S.; McAnally, M. O.; Chapman, C. T.; Henry, A.-I.; Schatz, G. C.; Van Duyne, R. P. Single-Molecule Chemistry with Surface- and Tip-Enhanced Raman Spectroscopy. *Chem. Rev.* **2016**, DOI: 10.1021/acs.chemrev.6b00552.

(4) Hayazawa, N.; Yano, T.; Watanabe, H.; Inouye, Y.; Kawata, S. Detection of an Individual Single-Wall Carbon Nanotube by Tip-Enhanced Near-Field Raman Spectroscopy. *Chem. Phys. Lett.* **2003**, *376*, 174−180.

(5) Schäffel, F.; Wilson, M.; Bachmatiuk, A.; Rümmeli, M. H.; Queitsch, U.; Rellinghaus, B.; Briggs, G. A. D.; Warner, J. H. Atomic Resolution Imaging of the Edges of Catalytically Etched Suspended Few-Layer Graphene. *ACS Nano* **2011**, *5*, 1975−1983.

(6) Stadler, J.; Schmid, T.; Zenobi, R. Nanoscale Chemical Imaging of Single-Layer Graphene. *ACS Nano* **2011**, *5*, 8442−8448.

(7) Yano, T.-A.; Verma, P.; Saito, Y.; Ichimura, T.; Kawata, S. Pressure-Assisted Tip-Enhanced Raman Imaging at a Resolution of a Few Nanometres. *Nat. Photonics* **2009**, *3*, 473−477.

(8) Peica, N.; Thomsen, C.; Maultzsch, J. Studying the Local Character of Raman Features of Single-Walled Carbon Nanotubes along a Bundle Using TERS. *Nanoscale Res. Lett.* **2011**, *6*, 174.

(9) van Schrojenstein Lantman, E. M.; Deckert-Gaudig, T.; Mank, A. J. G.; Deckert, V.; Weckhuysen, B. M. Catalytic Processes Monitored at the Nanoscale with Tip-Enhanced Raman Spectroscopy. *Nat. Nanotechnol.* **2012**, *7*, 583−586.

(10) Kurouski, D.; Mattei, M.; Duyne, R. P. V. Probing Redox Reactions at the Nanoscale with Electrochemical Tip-Enhanced Raman Spectroscopy. *Nano Lett.* **2015**, *15*, 7956−7962.

(11) Klingsporn, J. M.; Jiang, N.; Pozzi, E. A.; Sonntag, M. D.; Chulhai, D.; Seideman, T.; Jensen, L.; Hersam, M. C.; Duyne, R. P. V. Intramolecular Insight into Adsorbate-Substrate Interactions via Low-Temperature, Ultrahigh-Vacuum Tip-Enhanced Raman Spectroscopy. *J. Am. Chem. Soc.* **2014**, *136*, 3881−3887.

(12) Zeng, Z.-C.; Huang, S.-C.; Wu, D.-Y.; Meng, L.-Y.; Li, M.-H.; Huang, T.-X.; Zhong, J.-H.; Wang, X.; Yang, Z.-L.; Ren, B. Electrochemical Tip-Enhanced Raman Spectroscopy. *J. Am. Chem. Soc.* **2015**, *137*, 11928−11931.

(13) Zhong, J.-H.; Jin, X.; Meng, L.; Wang, X.; Su, H.-S.; Yang, Z.-L.; Williams, C. T.; Ren, B. Probing the Electronic and Catalytic Properties of a Bimetallic Surface with 3 nm Resolution. *Nat. Nanotechnol.* **2016**, *12*, 132−136.

(14) Liu, Z.; Ding, S.-Y.; Chen, Z.-B.; Wang, X.; Tian, J.-H.; Anema, J. R.; Zhou, X.-S.; Wu, D.-Y.; Mao, B.-W.; Xu, X.; Ren, B.; Tian, Z.-Q. Revealing the Molecular Structure of Single-Molecule Junctions in Different Conductance States by Fishing-Mode Tip-Enhanced Raman Spectroscopy. *Nat. Commun.* **2011**, *2*, 305.

(15) Mattei, M.; Kang, G.; Goubert, G.; Chulhai, D. V.; Schatz, G. C.; Jensen, L.; Duyne, R. P. V. Tip-Enhanced Raman Voltammetry: Coverage Dependence and Quantitative Modeling. *Nano Lett.* **2017**, *17*, 590−596.

(16) Domke, K. F.; Zhang, D.; Pettinger, B. Tip-Enhanced Raman Spectra of Picomole Quantities of DNA Nucleobases at Au(111). *J. Am. Chem. Soc.* **2007**, *129*, 6708−6709.

(17) Opilik, L.; Bauer, T.; Schmid, T.; Stadler, J.; Zenobi, R. Nanoscale Chemical Imaging of Segregated Lipid Domains Using Tip-Enhanced Raman Spectroscopy. *Phys. Chem. Chem. Phys.* **2011**, *13*, 9978−9981.

(18) Deckert-Gaudig, T.; Kämmer, E.; Deckert, V. Tracking of Nanoscale Structural Variations on a Single Amyloid Fibril with Tip-Enhanced Raman Scattering. *J. Biophotonics* **2012**, *5*, 215−219.

(19) Pozzi, E. A.; Sonntag, M. D.; Jiang, N.; Klingsporn, J. M.; Hersam, M. C.; Van Duyne, R. P. Tip-Enhanced Raman Imaging: An Emergent Tool for Probing Biology at the Nanoscale. *ACS Nano* **2013**, *7*, 885−888.

(20) Rusciano, G.; Zito, G.; Isticato, R.; Sirec, T.; Ricca, E.; Bailo, E.; Sasso, A. Nanoscale Chemical Imaging of *Bacillus subtilis* Spores by Combining Tip-Enhanced Raman Scattering and Advanced Statistical Tools. *ACS Nano* **2014**, *8*, 12300−12309.

(21) Neacsu, C. C.; Dreyer, J.; Behr, N.; Raschke, M. B. Scanning-Probe Raman Spectroscopy with Single-Molecule Sensitivity. *Phys. Rev. B: Condens. Matter Mater. Phys.* **2006**, *73*, 193406.

(22) Stöckle, R. M.; Suh, Y. D.; Deckert, V.; Zenobi, R. Nanoscale Chemical Analysis by Tip-Enhanced Raman Spectroscopy. *Chem. Phys. Lett.* **2000**, *318*, 131−136.

(23) Hayazawa, N.; Inouye, Y.; Sekkat, Z.; Kawata, S. Near-Field Raman Scattering Enhanced by a Metallized Tip. *Chem. Phys. Lett.* **2001**, *335*, 369−374.

(24) Zhang, W.; Yeo, B. S.; Schmid, T.; Zenobi, R. Single Molecule Tip-Enhanced Raman Spectroscopy with Silver Tips. *J. Phys. Chem. C* **2007**, *111*, 1733−1738.

(25) Steidtner, J.; Pettinger, B. Tip-Enhanced Raman Spectroscopy and Microscopy on Single Dye Molecules with 15 nm Resolution. *Phys. Rev. Lett.* **2008**, *100*, 236101.

(26) Stadler, J.; Schmid, T.; Zenobi, R. Nanoscale Chemical Imaging Using Top-Illumination Tip-Enhanced Raman Spectroscopy. *Nano Lett.* **2010**, *10*, 4514−4520.

(27) Sonntag, M. D.; Klingsporn, J. M.; Garibay, L. K.; Roberts, J. M.; Dieringer, J. A.; Seideman, T.; Scheidt, K. A.; Jensen, L.; Schatz, G. C.; Van Duyne, R. P. Single-Molecule Tip-Enhanced Raman Spectroscopy. *J. Phys. Chem. C* **2012**, *116*, 478−483.

(28) Chen, C.; Hayazawa, N.; Kawata, S. A 1.7 nm Resolution Chemical Analysis of Carbon Nanotubes by Tip-Enhanced Raman Imaging in the Ambient. *Nat. Commun.* **2014**, *5*, 3312.

(29) Jiang, N.; Chiang, N.; Madison, L. R.; Pozzi, E. A.; Wasielewski, M. R.; Seideman, T.; Ratner, M. A.; Hersam, M. C.; Schatz, G. C.; Van Duyne, R. P. Nanoscale Chemical Imaging of a Dynamic Molecular Phase Boundary with Ultrahigh Vacuum Tip-Enhanced Raman Spectroscopy. *Nano Lett.* **2016**, *16*, 3898−3904.

(30) Zhang, R.; Zhang, Y.; Dong, Z. C.; Jiang, S.; Zhang, C.; Chen, L. G.; Zhang, L.; Liao, Y.; Aizpurua, J.; Luo, Y.; Yang, J. L.; Hou, J. G. Chemical Mapping of a Single Molecule by Plasmon-Enhanced Raman Scattering. *Nature* **2013**, *498*, 82−86.

(31) Jiang, S.; Zhang, Y.; Zhang, R.; Hu, C.; Liao, M.; Luo, Y.; Yang, J.; Dong, Z.; Hou, J. G. Distinguishing Adjacent Molecules on a Surface Using Plasmon-Enhanced Raman Scattering. *Nat. Nanotechnol.* **2015**, *10*, 865−869.

(32) Chiang, N.; Chen, X.; Goubert, G.; Chulhai, D. V.; Chen, X.; Pozzi, E. A.; Jiang, N.; Hersam, M. C.; Seideman, T.; Jensen, L.; Van Duyne, R. P. Conformational Contrast of Surface-Mediated Molecular Switches Yields Ångstrom-Scale Spatial Resolution in Ultrahigh Vacuum Tip-Enhanced Raman Spectroscopy. *Nano Lett.* **2016**, *16*, 7774−7778.

(33) Hayazawa, N.; Inouye, Y.; Sekkat, Z.; Kawata, S. Metallized Tip Amplification of Near-Field Raman Scattering. *Opt. Commun.* **2000**, *183*, 333−336.

(34) Anderson, M. S. Locally Enhanced Raman Spectroscopy with an Atomic Force Microscope. *Appl. Phys. Lett.* **2000**, *76*, 3130−3132.

(35) Duan, S.; Tian, G.; Ji, Y.; Shao, J.; Dong, Z.; Luo, Y. Theoretical Modeling of Plasmon-Enhanced Raman Images of a Single Molecule with Subnanometer Resolution. *J. Am. Chem. Soc.* **2015**, *137*, 9515−9518.

(36) Duan, S.; Tian, G.; Luo, Y. Visualization of Vibrational Modes in Real Space by Tip-Enhanced Non-Resonant Raman Spectroscopy. *Angew. Chem., Int. Ed.* **2016**, *55*, 1041−1045.

(37) Halas, N. J.; Lal, S.; Chang, W.-S.; Link, S.; Nordlander, P. Plasmons in Strongly Coupled Metallic Nanostructures. *Chem. Rev.* **2011**, *111*, 3913−3961.
(38) Savage, K. J.; Hawkeye, M. M.; Esteban, R.; Borisov, A. G.; Aizpurua, J.; Baumberg, J. J. Revealing the Quantum Regime in Tunnelling Plasmonics. *Nature* **2012**, *491*, 574−577.
(39) Tan, S. F.; Wu, L.; Yang, J. K. W.; Bai, P.; Bosman, M.; Nijhuis, C. A. Quantum Plasmon Resonances Controlled by Molecular Tunnel Junctions. *Science* **2014**, *343*, 1496−1499.
(40) Esteban, R.; Borisov, A. G.; Nordlander, P.; Aizpurua, J. Bridging Quantum and Classical Plasmonics with a Quantum-Corrected Model. *Nat. Commun.* **2012**, *3*, 825.
(41) Zhu, W.; Esteban, R.; Borisov, A. G.; Baumberg, J. J.; Nordlander, P.; Lezec, H. J.; Aizpurua, J.; Crozier, K. B. Quantum Mechanical Effects in Plasmonic Structures with Subnanometre Gaps. *Nat. Commun.* **2016**, *7*, 11495.
(42) Payton, J. L.; Morton, S. M.; Moore, J. E.; Jensen, L. A Hybrid Atomistic Electrodynamics−Quantum Mechanical Approach for Simulating Surface-Enhanced Raman Scattering. *Acc. Chem. Res.* **2014**, *47*, 88−99.
(43) Barbry, M.; Koval, P.; Marchesin, F.; Esteban, R.; Borisov, A. G.; Aizpurua, J.; Sánchez-Portal, D. Atomistic Near-Field Nanoplasmonics: Reaching Atomic-Scale Resolution in Nanooptics. *Nano Lett.* **2015**, *15*, 3410−3419.
(44) Trautmann, S.; Aizpurua, J.; Götz, I.; Undisz, A.; Dellith, J.; Schneidewind, H.; Rettenmayr, M.; Deckert, V. A Classical Description of Subnanometer Resolution by Atomic Features in Metallic Structures. *Nanoscale* **2017**, *9*, 391−401.
(45) Latorre, F.; Kupfer, S.; Bocklitz, T.; Kinzel, D.; Trautmann, S.; Gräfe, S.; Deckert, V. Spatial Resolution of Tip-Enhanced Raman Spectroscopy − DFT Assessment of the Chemical Effect. *Nanoscale* **2016**, *8*, 10229−10239.
(46) Jensen, L. L.; Jensen, L. Electrostatic Interaction Model for the Calculation of the Polarizability of Large Noble Metal Nanoclusters. *J. Phys. Chem. C* **2008**, *112*, 15697−15703.
(47) Jensen, L. L.; Jensen, L. Atomistic Electrodynamics Model for Optical Properties of Silver Nanoclusters. *J. Phys. Chem. C* **2009**, *113*, 15182−15190.
(48) Chen, X.; Moore, J.; Zekarias, M.; Jensen, L. Atomistic Electrodynamics Simulations of Bare and Ligand-Coated Nanoparticles in the Quantum Size Regime. *Nat. Commun.* **2015**, *6*, 8921.
(49) Ayars, E. J.; Hallen, H. D.; Jahncke, C. L. Electric Field Gradient Effects in Raman Spectroscopy. *Phys. Rev. Lett.* **2000**, *85*, 4180−4183.
(50) Neacsu, C. C.; Berweger, S.; Raschke, M. B. Tip-Enhanced Raman Imaging and Spectroscopy: Sensitivity, Symmetry and Selection Rules. *NanoBiotechnology* **2008**, *3*, 172−196.
(51) Neugebauer, J.; Reiher, M.; Kind, C.; Hess, B. A. Quantum chemical calculation of vibrational spectra of large molecules - Raman and IR spectra for Buckminsterfullerene. *J. Comput. Chem.* **2002**, *23*, 895−910.
(52) Benz, F.; Schmidt, M. K.; Dreismann, A.; Chikkaraddy, R.; Zhang, Y.; Demetriadou, A.; Carnegie, C.; Ohadi, H.; de Nijs, B.; Esteban, R.; Aizpurua, J.; Baumberg, J. J. Single-Molecule Optomechanics in "Picocavities. *Science* **2016**, *354*, 726−729.
(53) Chen, X.; Jensen, L. Understanding the Shape Effect on the Plasmonic Response of Small Ligand Coated Nanoparticles. *J. Opt.* **2016**, *18*, 074009.
(54) Le, F.; Brandl, D. W.; Urzhumov, Y. A.; Wang, H.; Kundu, J.; Halas, N. J.; Aizpurua, J.; Nordlander, P. Metallic Nanoparticle Arrays: A Common Substrate for Both Surface-Enhanced Raman Scattering and Surface-Enhanced Infrared Absorption. *ACS Nano* **2008**, *2*, 707−718.
(55) Sass, J. K.; Neff, H.; Moskovits, M.; Holloway, S. Electric Field Gradient Effects on the Spectroscopy of Adsorbed Molecules. *J. Phys. Chem.* **1981**, *85*, 621−623.
(56) Wolkow, R. A.; Moskovits, M. Benzene Adsorbed on Silver: An Electron Energy Loss and Surface-enhanced Raman Study. *J. Chem. Phys.* **1986**, *84*, 5196−5199.
(57) Aikens, C. M.; Madison, L. R.; Schatz, G. C. Raman Spectroscopy: The Effect of Field Gradient on SERS. *Nat. Photonics* **2013**, *7*, 508−510.
(58) Takase, M.; Ajiki, H.; Mizumoto, Y.; Komeda, K.; Nara, M.; Nabika, H.; Yasuda, S.; Ishihara, H.; Murakoshi, K. Selection-rule Breakdown in Plasmon-induced Electronic Excitation of an Isolated Single-walled Carbon Nanotube. *Nat. Photonics* **2013**, *7*, 550−554.
(59) Chulhai, D. V.; Jensen, L. Determining Molecular Orientation With Surface-Enhanced Raman Scattering Using Inhomogenous Electric Fields. *J. Phys. Chem. C* **2013**, *117*, 19622−19631.
(60) Liljeroth, P.; Repp, J.; Meyer, G. Current-Induced Hydrogen Tautomerization and Conductance Switching of Naphthalocyanine Molecules. *Science* **2007**, *317*, 1203−1206.
(61) Auwärter, W.; Seufert, K.; Bischoff, F.; Ecija, D.; Vijayaraghavan, S.; Joshi, S.; Klappenberger, F.; Samudrala, N.; Barth, J. V. A Surface-Anchored Molecular Four-Level Conductance Switch Based on Single Proton Transfer. *Nat. Nanotechnol.* **2011**, *7*, 41−46.
(62) te Velde, G.; Bickelhaupt, F. M.; Baerends, E. J.; Fonseca Guerra, C.; van Gisbergen, S. J. A.; Snijders, J. G.; Ziegler, T. Chemistry with ADF. *J. Comput. Chem.* **2001**, *22*, 931−967.
(63) Fonseca Guerra, C.; Snijders, J. G.; te Velde, G.; Baerends, E. J. Towards an order-N DFT method. *Theor. Chem. Acc.* **1998**, *99*, 391−403.
(64) Baerends, E. J.; Ziegler, T.; Atkins, A. J.; Autschbach, J.; Bashford, D.; Bérces, A.; Bickelhaupt, F. M.; Bo, C.; Boerritger, P. M.; Cavallo, L.; Chong, D. P.; Chulhai, D. V.; Deng, L.; Dickson, R. M.; Dieterich, J. M.; Ellis, D. E.; van Faassen, M.; Ghysels, A.; Giammona, A.; van Gisbergen, S. J. A.; et al. *ADF2016*, SCM, Theoretical Chemistry, Vrije Universiteit: Amsterdam, The Netherlands, https://www.scm.com.
(65) Becke, A. D. Density-Functional Exchange-Energy Approximation with Correct Asymtotic-Behavior. *Phys. Rev. A: At., Mol., Opt. Phys.* **1988**, *38*, 3098−3100.
(66) Perdew, J. P. Density-functional Approximation for the Correlation Energy of the Inhomogeneous Electron Gas. *Phys. Rev. B: Condens. Matter Mater. Phys.* **1986**, *33*, 8822−8824.
(67) Zhao, L.; Jensen, L.; Schatz, G. C. Pyridine-Ag20 Cluster: A Model System for Studying Surface-Enhanced Raman Scattering. *J. Am. Chem. Soc.* **2006**, *128*, 2911−2919.
(68) Jensen, L.; Autschbach, J.; Schatz, G. C. Finite Lifetime Effects on the Polarizability Within Time-dependent Density-functional Theory. *J. Chem. Phys.* **2005**, *122*, 224115.
(69) Jensen, L.; Zhao, L. L.; Autschbach, J.; Schatz, G. C. Theory and Method for Calculating Resonance Raman Scattering from Resonance Polarizability Derivatives. *J. Chem. Phys.* **2005**, *123*, 174110.
(70) Zhao, L. L.; Jensen, L.; Schatz, G. C. Surface-Enhanced Raman Scattering of Pyrazine at the Junction between Two Ag20 Nanoclusters. *Nano Lett.* **2006**, *6*, 1229−1234.
(71) Jensen, L.; Schatz, G. C. Resonance Raman Scattering of Rhodamine 6G as Calculated Using Time-Dependant Density Functional Theory. *J. Phys. Chem. A* **2006**, *110*, 5973−5977.
(72) Johnson, P. B.; Christy, R. W. Optical Constants of the Noble Metals. *Phys. Rev. B* **1972**, *6*, 4370−4379.
(73) Humphrey, W.; Dalke, A.; Schulten, K. VMD: Visual Molecular Dynamics. *J. Mol. Graphics* **1996**, *14*, 33−38.

DOI: 10.1021/acsnano.7b02058
ACS Nano 2017, 11, 5094−5102